7. Huss, G. in *Astrophysical Implications of the Laboratory Study of Presolar Materials* (eds Bernatowicz, T. & Zinner, E.) 721–748 (AIP Press, New York, 1997).

8. Bradley, J. P. & Brownlee, D. E. Cometary particles: thin-sectioning and electron-beam analysis. *Science* **231**, 1542–1544 (1984).

9. Brownlee, D. E. *et al.* Identification of individual cometary IDPs by thermally stepped He release. *Lunar Planet Sci.* **XXVI**, 183–184 (1995).

10. Van Kerckhoven, C., Tielens, A. G. G. M. & Waelkens, C. Nanodiamonds around HD 97048 and Elias 1. *Astron. Astrophys.* **384**, 568–584 (2002).

11. Hill, H. G. M., Grady, C. A., Nuth, J. A., Hallenbeck, S. L. & Sitko, M. L. Constraints on nebular dynamics and chemistry based on observations of annealed magnesium silicate grains in comets and in disks around Herbig Ae and Be stars. *Proc. Natl Acad. Sci. USA* **98**, 2182–2187 (2001).

12. Bernatowicz, T. J. & Gibbons, P. C. Electron energy-loss spectroscopy of interstellar diamonds. *Astrophys. J.* **359**, 246–255 (1990).

13. Brownlee, D. E., Joswiak, D. J., Bradley, J. P., Gezo, J. C. & Hill, H. G. M. Spatially resolved acid dissolution of IDPs: the state of carbon and the abundance of diamonds in the dust. *Lunar Planet. Sci.* **XXXI**, 1921–1922 (2000).

14. Messenger, S. Identification of molecular cloud material in interplanetary dust particles. *Nature* **404**, 968–971 (2000).

15. Bradley, J. P. & Brownlee, D. E. An interplanetary dust particle linked to type CM meteorites and an asteroidal origin. *Science* **251**, 489–596 (1992).

16. Thomas, K. L. *et al.* An asteroidal breccia: The anatomy of a cluster IDP. *Geochim. Cosmochim. Acta* **59**, 2797–2815 (1995).

17. Luu, J. X. Spectral diversity among the nuclei of comets. *Icarus* **104**, 138–148 (1993).

18. Russell, S. S., Arden, J. W. & Pillinger, C. T. A carbon and nitrogen isotope study of diamond from primitive meteorites. *Meteorit. Planet. Sci.* **31**, 343–355 (1996).

19. Huss, G. R. & Lewis, R. S. Noble gases in presolar diamonds. I, Three distinct components and their implications for diamond origins. *Meteoritics* **29**, 791–810 (1994).

20. Sylvester, R. J. in *Solid Interstellar Matter: The ISO Revolution* (eds d'Hendecourt, L., Joblin, C. & Jones, A.) 263–276 (Springer, New York, 1999).

21. Hill, H. G. M., Jones, A. P. & d'Hendecourt, L. B. Diamonds in carbon-rich proto-planetary nebulae. *Astron. Astrophys.* **336**, L41–L44 (1998).

22. Guillois, O., Ledoux, G. & Reynaud, C. Diamond infrared emission bands in circumstellar media. *Astrophys. J.* **521**, L133–L136 (1999).

23. Lodders, K. & Palme, H. in *Protostars and Planets IV* (eds Krot, A. N. & Fegley, B.) 1019–1053 (Univ. Arizona Press, Tucson, 2000).

24. Howard, W. *et al.* Synthesis of diamond powder in acetylene oxygen plasma. *J. Appl. Phys.* **68**, 1247–1251 (1990).

25. Liou, J.-C., Zook, H. A. & Dermott, S. F. Kuiper belt dust grains as a source of interplanetary dust particles. *Icarus* **124**, 429–440 (1996).

26. Bradley, J. P. Chemically anomalous, pre-accretionally irradiated grains in interplanetary dust particles from comets. *Science* **265**, 925–927 (1992).

27. Thomas, K. L., Blanford, G. E., Keller, L. P., Klöck, W. & McKay, D. S. Carbon abundance and silicate mineralogy of anhydrous interplanetary dust particles. *Geochim. Cosmochim. Acta* **57**, 1551–1566 (1993).

28. Schramm, L. S., Brownlee, D. E. & Wheelock, M. M. Major element compositions of stratospheric micrometeorites. *Meteoritics* **24**, 99–112 (1989).

### Competing interests statement

The authors declare that they have no competing financial interests.

Correspondence and requests for materials should be addressed to J.P.B. (e-mail: jbradley@igpp.ucllnl.org).

........................................................

# Phonon-enhanced light–matter interaction at the nanometre scale

**R. Hillenbrand, T. Taubner & F. Keilmann**

*Max-Planck-Institut für Biochemie, Abteilung Molekulare Strukturbiologie, 82152 Martinsried & Center for NanoScience, Ludwig-Maximilians-Universität, 80799 München, Germany*

.......................................................................................................................................................

**Optical near fields exist close to any illuminated object. They account for interesting effects such as enhanced pinhole transmission[1] or enhanced Raman scattering enabling single-molecule spectroscopy[2]. Also, they enable high-resolution (below 10 nm) optical microscopy[3–6]. The plasmon-enhanced near-field coupling between metallic nanostructures[7–9] opens new ways of designing optical properties[10–12] and of controlling light on the nanometre scale[13,14]. Here we study the strong enhancement of optical near-field coupling in the infrared by lattice vibrations (phonons) of polar dielectrics. We combine infrared spectroscopy with a near-field microscope that provides a confined field to probe the local interaction with a SiC sample. The phonon resonance occurs at 920 cm$^{-1}$. Within 20 cm$^{-1}$ of the resonance, the near-field signal increases 200-fold; on resonance, the signal exceeds by 20 times the value obtained with a gold sample. We find that phonon-enhanced near-field coupling is extremely sensitive to chemical and structural composition of polar samples, permitting nanometre-scale analysis of semiconductors and minerals. The excellent physical and chemical stability of SiC in particular may allow the design of nanometre-scale optical circuits for high-temperature and high-power operation.**

A recent approach to confining and guiding light uses the strong near fields of closely spaced metallic nanostructures[13,14]. In these structures, a collective motion of conduction electrons (the surface plasmon polariton[15], referred to here as "plasmon") becomes resonantly excited by visible light. The interparticle coupling by plasmons provides field confinement and photon transport over mesoscopic distances. An infrared counterpart to the surface plasmon polariton is the surface phonon polariton (referred to here as "phonon"), which has weaker damping[15] and thus offers the advantage of stronger and sharper optical resonances. We demonstrate this for the small-particle (Fröhlich[16]) resonance, by calculating the enhanced optical field $E_{loc}$ at the surface of an illuminated sphere with radius $a$ and dielectric function $\varepsilon_p$ (the incident field is $E_{in}$). In the electrostatic approximation (which is valid as we assume a particle size much smaller than the wavelength) the sphere's polarizability is given by

$$\alpha = 4\pi a^3 (\varepsilon_p - \varepsilon_m)/(\varepsilon_p + 2\varepsilon_m) \tag{1}$$

where $\varepsilon_m$ is the dielectric function of the embedding medium[17]. The local field enhancement $E_{loc}/E_{in} \propto \alpha$ has a resonance at a frequency determined by $\mathrm{Re}[\varepsilon_p(\omega)] = -2\varepsilon_m$ (note this condition can be fulfilled likewise by phonons, plasmons or excitons). By inserting dielectric data of metals[18] and SiC[19] into equation (1), we obtain the curves shown in Fig. 1, which clearly demonstrate that the infrared phonon resonance of a small polar-dielectric particle is much stronger and sharper than the plasmon resonance of an equally small metal particle. Accordingly, we propose phonon photonics as a concept in nanotechnology analogous to plasmon photonics. Compared to plasmon resonance (applied, for example, in small-particle sensors[20]), the sharper phonon resonance enables an even higher sensitivity to environmental changes affecting $\varepsilon_m$, such as molecular adsorption. Phonon resonance also responds to changes in the lattice parameters affecting $\varepsilon_p$. This could be used to detect variations in local temperature and pressure. The necessary infrared frequencies could be supplied by quantum cascade lasers[21,22], which
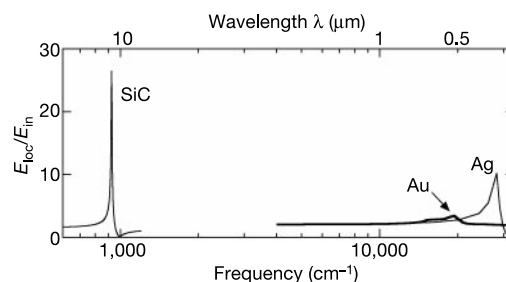


**Figure 1** Calculated field enhancement $E_{loc}/E_{in}$ due to Fröhlich resonance at the surface of a 10-nm-diameter sphere. The infrared lattice vibration (phonon) of a polar dielectric (SiC) induces a considerably stronger near-field amplitude than the green/blue electronic excitation (plasmon) of a noble metal (Au, Ag).

**159**

are readily tailored to match the characteristic phonon frequencies of polar materials that include III–V and II–VI semiconductors.
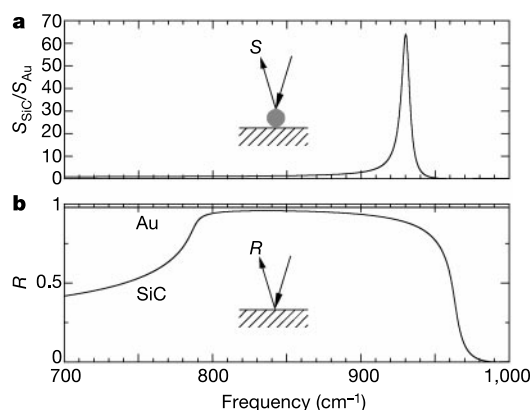
Here we focus on the phonon enhancement of the optical interaction between two objects at a nanometric distance from each other. Localized optical interaction has become accessible to experimentation by the recent advance of the 'apertureless', scattering-type scanning near-field optical microscope (s-SNOM)[3–6,23,24], in which near-field coupling is the essential contrast mechanism[5,6,23,24]. We therefore consider the configuration[15,25] of a small sphere with radius $a$ at a small distance $z$ from a plane sample (Fig. 2a inset), the former representing the probing tip of the s-SNOM. The electric field is polarized perpendicularly to the sample surface. The sphere induces an image dipole in the sample, with polarizability $\alpha\beta$ where

$$\beta = (\varepsilon_s - 1)/(\varepsilon_s + 1) \qquad (2)$$

is the surface response function, $\varepsilon_s$ being the dielectric function of the sample. Note that the image dipole can become resonant by the dielectric value of the sample alone, at $\mathrm{Re}[\varepsilon_s(\omega)] = -1$, independently of whether the sphere is resonant or not. The near-field interaction between both dipoles is described by an effective polarizability, in electrostatic approximation[6]:

$$\alpha_{\mathrm{eff}} = \frac{\alpha(1 + \beta)}{1 - \frac{\alpha\beta}{16\pi(a+z)^3}} \qquad (3)$$

A resonant near-field interaction thus originates from the dielectric resonance of either a polar sphere (equation (1)) or a polar sample (equation (2)). The interaction plays no key role in the generation of the resonance, but modifies strength and spectral position. Without losing generality, we can show the phonon-enhanced interaction by considering the case of a resonant sample material. This choice simplifies an experimental comparison between a phonon-active material (SiC) and a non-resonant reference material (Au). The near-field interaction (equation (3)) is experimentally accessible by measuring the scattered intensity $S$ of the coupled system, which depends on $\alpha_{\mathrm{eff}}$ as $S \propto |\alpha_{\mathrm{eff}}|^2$. An evaluation of $S$ for Au and SiC samples is given in Fig. 2a, with Pt as (non-resonant) sphere material. The result for SiC exhibits a very sharp resonance at $930\,\mathrm{cm}^{-1}$ (where $\mathrm{Re}[\varepsilon_s(\omega)] \approx -1.7$), exceeding the value of Au by nearly two orders of magnitude, in contrast to the far-field interaction (Fig. 2b). In Fig. 2b, the phonon-induced 'reststrahlen' reflectivity band of SiC extends from 790 to $950\,\mathrm{cm}^{-1}$, a region where $\mathrm{Re}(\varepsilon_s) < 0$ forbids bulk propagation. The near-field probing singles out a sharp resonance within the phonon band, resulting in a spectral response very different from the far-field response. Such a spectral narrowing had been predicted

earlier for the near field of SiC[25,26]. In the case of ref. 26, it occurs at the asymptotic frequency of the phonon dispersion, given by $\mathrm{Re}[\varepsilon_s(\omega)] = -1$, owing to thermally excited phonons.

The experimental proof of the predicted phonon-resonant near-field interaction is carried out by inspecting a flat SiC surface with our infrared s-SNOM[6,24] (Fig. 3a). Here a sharp tip at the end of a cantilever takes the role of the sphere of the model above. The instrument is basically an atomic force microscope, where the Pt-coated tip (radius $\sim$20 nm) maps the topography of a scanned sample. The tip is illuminated by focused infrared light from a line-tunable $CO_2$ laser or a quantum cascade laser. $E_{\mathrm{in}}$ is polarized in the $y$–$z$ plane. Back-scattered light is collected through the focusing cassegrainian objective, and detected interferometrically (details to be published elsewhere) to register the scattered amplitude $s = \sqrt{S} \propto |\alpha_{\mathrm{eff}}|$ that directly measures the local near-field interaction between tip and sample surface. To assess the pure near-field interaction, it is essential to suppress unavoidable background light scattered from the tip's shaft and cantilever. Our solution is to use the tapping mode, where the cantilever vibrates at its resonance frequency $\Omega$ so that the tip–sample separation $z$ oscillates between 0 and $\sim$40 nm—that is, with amplitude $\Delta z \approx 20\,\mathrm{nm}$. Owing to the nonlinear $z$-dependence, the near-field interaction (equation (3)) and thus $s$ become modulated at higher harmonics $n\Omega$ ($n > 1$), but the background scattering is not modulated in this way. Lock-in detection at $n\Omega$ ($n = 2$ used in this work) can therefore suppress the background[5,23]. The sample is a polished, Acheson grade 6H-SiC crystal partly coated with a 10-nm-thick, nanostructured gold film[27]. A large number of infrared images are taken repeatedly of the same sample area, which contains both Au and SiC surfaces, at many wavelength settings of the laser.

The infrared image brightness $s$ (Fig. 3c) maps the local near-field coupling between tip and sample, and thus allows us to directly compare different sample materials. Indeed, near the frequency of the predicted phonon resonance (Fig. 2a and image at $929\,\mathrm{cm}^{-1}$) SiC appears much brighter than Au. When changing frequency, the signal changes on SiC but not on Au. A 5% relative frequency shift (image at $978\,\mathrm{cm}^{-1}$) is sufficient to reverse contrast and even lose the signal in the instrument's noise. These two images already demonstrate a strong phonon effect in SiC. To quantify the phonon
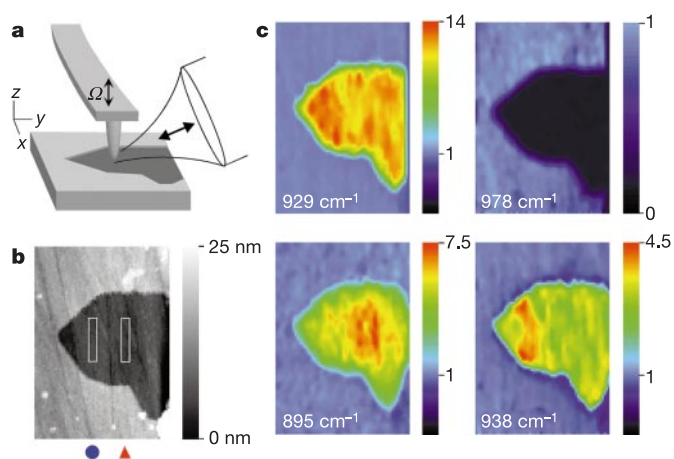
**Figure 2** Enhancement and narrowing of a phonon-induced spectral response by the near-field probing process. **a**, Intensity $S$ of scattering from a small Pt probe particle of radius $a \ll \lambda$ in contact with a SiC surface (relative to an Au surface); **b**, far-field reflectivity $R$ of SiC (reststrahlen band) and of Au (nearly perfect mirror).

**Figure 3** Experimental scheme (**a**) and images (**b,c**) taken with a scattering-type mid-infrared scanning near-field microscope (s-SNOM). The topography (**b**) shows a partly Au-covered SiC sample (image size $1.6 \times 2.3\,\mu\mathrm{m}^2$). Two rectangles mark areas used for data extraction. The infrared near-field images (**c**) display the scattering amplitude $s$ taken at different frequencies of illumination as indicated, and are scaled such that Au appears blue. On phonon resonance, the SiC area appears much brighter than the surrounding Au ($929\,\mathrm{cm}^{-1}$). The contrast reverses at $978\,\mathrm{cm}^{-1}$. Two examples taken on either side of the resonance ($895\,\mathrm{cm}^{-1}$ and $938\,\mathrm{cm}^{-1}$) indicate a systematic local variation in the infrared images (see text).

enhancement in detail, we extract two values of $s_{SiC}$ from an infrared image by averaging over rectangular areas indicated in Fig. 3b. We normalize to the value of Au to obtain two values of $s_{SiC}/s_{Au}$ from each infrared image, and plot them in a spectral diagram (Fig. 4). The experimental data trace out and resolve a resonance curve over a high dynamic range, which extends at its maximum 20-fold above the near-field coupling observed on Au. The resonance is accompanied by a minimum more than 10 times below the value for Au. Gaps in the spectrum are due to the tuning capability of our gas lasers operating with $^{12}C^{16}O_2$ and $^{13}C^{16}O_2$ fillings, or to undetectably small signals on SiC as at 968 and 978 cm$^{-1}$. A near-field image that we have taken with a quantum cascade laser (supplied by C. Gmachl) yields a corresponding value of $s_{SiC}/s_{Au} = 0.3$ at 1,360 cm$^{-1}$.
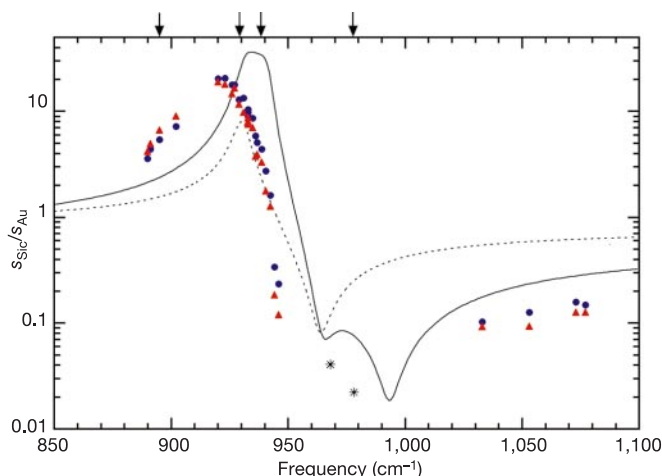
To compare our findings with theory, we recall the prediction (Fig. 2a) calculated from equation (3), and plot it as the dashed curve in Fig. 4. However, we have to take account of the experimental procedure of tip vibration and second-harmonic signal demodulation. For this simulation, one parameter is to be taken from the experiment—the relative tapping amplitude $\Delta z/a$. Assuming $\Delta z/a = 1$, we calculate the solid curve in Fig. 4, which follows the overall behaviour of the dashed curve but which exhibits a higher dynamic range (a systematic instrumental effect noted before[23]) and a broadening. Comparing now the solid curve with the experimental data, we find a strong resonance in both. Discrepancies such as a factor of two in the resonance enhancement and a frequency shift of about 15 cm$^{-1}$ are relatively small. These may call for a refinement of the theory by using a more realistic tip geometry (an example of tip-shape-dependent scattering is found in ref. 28) and a multipolar, electrodynamic formulation. However, the experimental data agree well with the narrow shape and the high dynamic range (three orders of magnitude in amplitude, that is, six orders in intensity) predicted by our model calculation, and thus verify the phonon enhancement of near-field coupling.

The images (Fig. 3c) are direct evidence that infrared spectroscopy is possible with excellent spatial resolution of $<\lambda/100$. This proves that the phonon-enhanced near-field interaction is highly localized. A close inspection of the infrared images reveals a substructure on SiC that depends on frequency (not observed on

Au). The signal at 895 cm$^{-1}$ is about 20% smaller in the left-hand third compared to the rest of the SiC area, but about 20% larger at 938 cm$^{-1}$. Indeed, the spectra (Fig. 4) extracted from the rectangles in Fig. 3c reveal a systematic frequency-dependent behaviour. At frequencies below resonance, the red triangles are above the blue dots, and this reverses above resonance, indicating a frequency shift of about 2 cm$^{-1}$ between the two sample locations. We take this as experimental evidence of a local variation of the dielectric function, expressing a variation in the physical structure or chemical composition of the sample. This could be due to polishing damage, impurity or doping. Certainly the sharpness of the phonon-enhanced near-field resonance offers extremely high sensitivity in detecting local material inhomogeneities by s-SNOM, an application that reaches far beyond the s-SNOM's demonstrated nanoscale mapping of chemical composition[5,6,23,24]. The resonance could be used to map crystallinity, dislocations, and profiles of stress or doping. With an experimental steepness of 1.2 dB per cm$^{-1}$, a single-frequency mapping at 940 cm$^{-1}$ (Fig. 4) would detect, under the assumption of 3% instrumental noise, a local variation of the resonance frequency as small as 0.1 cm$^{-1}$—that is, a relative change as small as $1 \times 10^{-4}$.

A technological application of the present work might be the use of SiC to provide durable, long-term, high-density optical read-only memory (ROM). Phonon enhancement could supply strong signals, enabling a fast near-field read-out of even 10-nm bits, equivalent to a storage density near 1 Tbit inch$^{-2}$. Also, sharp tips made out of SiC could be durable probes for infrared s-SNOM, with the added benefit that stronger signals might push the resolution limit well below 10 nm. The extreme infrared field strengths to be expected from phonon enhancement in narrow gaps between polar nanoparticles, exceeding those demonstrated for plasmon particles[2,9], may bring new opportunities to high-field nonlinear physics. □

1. Ebbesen, T. W., Lezec, H. J., Ghaemi, H. F., Thio, T. & Wolff, P. A. Extraordinary optical transmission through sub-wavelength hole arrays. *Nature* **391**, 667–669 (1998).
2. Xu, H., Bjerneld, E. J., Käll, M. & Börjesson, L. Spectroscopy of single hemoglobin molecules by surface enhanced Raman scattering. *Phys. Rev. Lett.* **83**, 4357–4360 (1999).
3. Specht, M., Pedarnig, J. D., Heckl, W. M. & Hänsch, T. W. Scanning plasmon near-field microscopy. *Phys. Rev. Lett.* **68**, 476–479 (1992).
4. Zenhausern, F., Martin, Y. & Wickramasinghe, H. K. Scanning interferometric apertureless microscopy: optical imaging at 10 Angstrom resolution. *Science* **269**, 1083–1085 (1995).
5. Hillenbrand, R. & Keilmann, F. Material-specific mapping of metal/semiconductor/dielectric nanosystems at 10 nm resolution by back-scattering near-field optical microscopy. *Appl. Phys. Lett.* **80**, 25–27 (2002).
6. Knoll, B. & Keilmann, F. Near-field probing of vibrational absorption for chemical microscopy. *Nature* **399**, 134–137 (1999).
7. Barnes, W. L. Fluorescence near interfaces: the role of photonic mode density. *J. Mod. Opt.* **45**, 661–699 (1998).
8. Colas des Francs, G. *et al.* Optical analogy to electronic quantum corrals. *Phys. Rev. Lett.* **86**, 4950–4953 (2001).
9. Hillenbrand, R. & Keilmann, F. Optical oscillation modes of plasmon particles observed in direct space by phase-contrast near-field microscopy. *Appl. Phys. B* **73**, 239–243 (2001).
10. Joannopoulos, J. D., Villeneuve, P. R. & Fan, S. Photonic crystal: putting new twists on light. *Nature* **386**, 143–149 (1997).
11. Pendry, J. B. Negative refraction makes a perfect lens. *Phys. Rev. Lett.* **85**, 3966–3969 (2000).
12. Smith, D. R., Padilla, W. J., Vier, D. C., Nemat-Nasser, S. C. & Schultz, P. G. Composite medium with simultaneously negative permeability and permittivity. *Phys. Rev. Lett.* **84**, 4184–4187 (2000).
13. Krenn, J. R. *et al.* Squeezing the optical near-field zone by plasmon coupling of metallic nanoparticles. *Phys. Rev. Lett.* **82**, 2590–2593 (1999).
14. Weeber, J.-C. *et al.* Optical addressing on the subwavelength scale. *Phys. Rev. E* **62**, 7381–7388 (2000).
15. Ruppin, R. J. in *Electromagnetic Surface Modes* (ed. Boardman, A. D.) 345–398 (Wiley, Chichester, 1982).
16. Fröhlich, H. *Theory of Dielectrics* (Clarendon, Oxford, 1949).
17. Jackson, J. D. *Classical Electrodynamics* (Wiley & Sons, New York, 1975).
18. Palik, E. W. *Handbook of Optical Constants of Solids* (Academic, San Diego, 1985).
19. Engelbrecht, F. & Helbig, R. Effect of crystal anisotropy on the infrared reflectivity of 6H-SiC. *Phys. Rev. B* **48**, 15698–15707 (1993).
20. Kreibig, U., Gartz, M. & Hilger, A. Mie resonances: Sensors for physical and chemical cluster interface properties. *Ber. Bunsenges. Phys. Chem.* **101**, 1593–1604 (1997).
21. Faist, J. *et al.* Quantum cascade laser. *Science* **264**, 553–556 (1994).
22. Beck, M. *et al.* Continuous wave operation of a mid-infrared semiconductor laser at room temperature. *Science* **295**, 301–305 (2002).
23. Hillenbrand, R. & Keilmann, F. Complex optical constants on a subwavelength scale. *Phys. Rev. Lett.* **85**, 3029–3032 (2000).

**Figure 4** Phonon-enhanced near-field response of SiC, normalized to Au. The data points are extracted from near-field images such as those of Fig. 3, the two symbols corresponding to two different sample locations marked there by rectangles. At two frequencies (968 and 978 cm$^{-1}$) $s_{SiC}$ is below the noise, which is marked instead by a black star. Arrows indicate the frequencies used for the images in Fig. 3c. The curves depict model predictions for the scattering amplitude $s$ of a small Pt particle in contact with a SiC surface, normalized to an Au surface, equivalent to Fig. 2a (dashed line), and the same modified to simulate the experimental procedure of sinusoidal tapping motion, assuming $\Delta z = a$, and of second-harmonic signal demodulation (solid line).

 **161**

24. Knoll, B. & Keilmann, F. Infrared conductivity mapping for nanoelectronics. *Appl. Phys. Lett.* **77**, 3980–3982 (2000).

25. Aravind, P. K. & Metiu, H. The effects of the interaction between resonances in the electromagnetic response of a sphere-plane structure; applications to surface enhanced spectroscopy. *Surf. Sci.* **124**, 506–528 (1983).

26. Shchegrov, A. V., Joulain, K., Carminati, R. & Greffet, J. J. Near-field spectral effects due to electromagnetic surface excitations. *Phys. Rev. Lett.* **85**, 1548–1551 (2000).

27. Hartmann, T., Kramer, A., Hillebrand, A., Guckenberger, R., et al. in *Procedures in Scanning Probe Microscopies* (ed. Colton, J. R.) 12–16 (Wiley, Chichester, 1998).

28. Aigouy, L. et al. Near-field optical spectroscopy using an incoherent light source. *Appl. Phys. Lett.* **76**, 397–399 (2000).

**Figure 1** Schematic diagram of the experimental apparatus. A PZT pusher capable of moving extremely slowly (a few Å s$^{-1}$) was used to drive the tip so that the sample could be maintained in a quasi-equilibrium state during compression. A balance (Sartorius, 1212 MP) was used to measure the pressure precisely by placing the sample on its top.
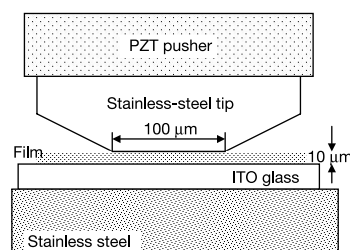
··········································

# Pressure-induced insulator–conductor transition in a photoconducting organic liquid-crystal film

**Chong-yang Liu & Allen J. Bard**

*Department of Chemistry and Biochemistry, The University of Texas at Austin, Austin, Texas 78712, USA*

**Intermolecular separation determines the extent of orbital overlap and thus the rate of electron transfer between neighbouring molecules in an organic crystal. If such a crystal is compressed, the resistivity decreases owing to a diminishing intermolecular distance[1]. Metal–insulator transitions have been observed by applying hydrostatic pressure to, for example, Langmuir films of metal nanoparticles[2,3]. But previous attempts to observe a clear transition point in organic crystals, such as anthracene and tetracene, were not successful owing to difficulties with electrically insulating the high-pressure cell[4]. Here we report a different approach by using a sample that is photoconductive and forms an organized film. A cylindrical tip (~100 μm in diameter) was used to compress the sample instead of a piston/cylinder structure, entirely eliminating the problem of electrical insulation. Furthermore, by illuminating the sample with a laser, the conductivity of the sample is increased by several orders of magnitude. By monitoring the photocurrent with sensitivity at the 10$^{-13}$ A level, changes in resistivity at very low pressure could be monitored. We observe a sharp increase in current that could indicate a transition from hopping to delocalized conduction.**

Zinc octakis(β-decoxyethyl)porphyrin (ZnODEP) was used as the sample. In the crystal, molecules are regularly stacked to form well-defined molecular columns. As the intercolumn separation is large (~24 Å), each column is fairly isolated electronically from a neighbouring column[5,6]. In fact, in the liquid-crystal state (95–147 °C), the column structure still remains in the discotic mesophase, although the long tails are disordered[5]. The molecule-to-molecule distance within the same column is also quite large (~4 Å). The structure of ZnODEP suggests that the solid should be relatively soft and easy to compress compared to other organic

crystals, such as anthracene. Films were made by a capillary filling of the substance in the molten state into empty ITO (indium tin oxide) sandwich cells as reported earlier[7,8]. The cells were then cooled to form a solid film, and separated to produce a free surface. As shown in previous work[7–9], the axes of the molecular columns are oriented perpendicular to the ITO surface, so that the pressure would mainly affect the intermolecular interactions within the same columns.

An argon-ion laser (100 mW at 488 nm, Melles Griot) was used to irradiate the film via a fibre optic through the ITO glass. The tip was made from a stainless-steel cylinder about 0.1 inch in diameter with one end tapered to a sharp point by mechanical polishing. The tip was then pressed against a stainless-steel or glass plate to flatten the end to about 100–150 μm diameter by applying very high pressure. The overall structure is tip/film/ITO (Fig. 1). The electrical contacts were made to both the ITO and the tip electrodes. The tip was pushed by a PZT (lead zirconate titanate) pusher (Burleigh) to compress the film. A micrometer was attached to the other end of the pusher for the initial rough adjustment of the distance between the tip and the film.

When the tip was brought into contact with the ZnODEP film, a steady photocurrent was observed under a fixed bias voltage of 3.2 V (with the tip negative). The magnitude of the photocurrent depended on the initial film thickness. A short-circuit photocurrent could also be detected, as reported earlier, with large-area ITO/ZnODEP/ITO sandwich cells[9–11]. This current is produced by preferential injection of photogenerated electrons from ZnODEP molecules into the illuminated ITO electrode, while holes hop through the film to the tip electrode. Note that the photocurrent started to increase immediately following the tip's forward move-
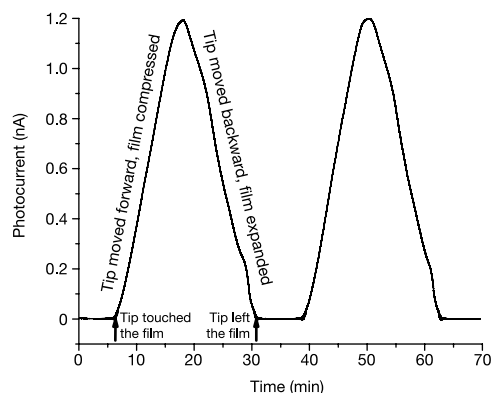


**Figure 2** Photocurrent as a function of compression and expansion of a ZnODEP film about 6 μm thick between ITO glass and a stainless-steel tip. The ITO glass was placed on a fixed stainless-steel platform, and the tip was moved at a rate of 4 nm s$^{-1}$. The film was irradiated from the ITO side with a fibre optic through a hole in the platform. A bias voltage of 3.2 V was applied between sample and tip, with the tip negative.